On Stability of Virtual Torsion Sensor for Control of Flexible Robotic Joints with Hysteresis

Michael Ruderman†*

† *Faculty of Engineering and Science, University of Agder, 4604-Norway*

SUMMARY

Aim of the virtual torsion sensor (VTS) is in observing the nonlinear deflection in the flexible joints of robotic manipulators and, by its use, improving positioning control of the joint load. This model-based approach utilizes the motor-side sensing only and, therefore, replaces the load-side encoders at nearly zero hardware costs. For being applied in the closed control loop, the stability and robustness of VTS are most crucial. This work extends the previous analysis by a general case of nonlinear joint stiffness with hysteresis and provides straightforward conditions with respect to the system dynamics. The dissipativity and passivity of the torsion-torque hysteresis map are analyzed and discussed in detail. The absolute stability of VTS inclusion into position control loop is shown based on the equivalent loop transformations and Popov criteria, including the sector conditions. Illustrative numerical examples of the control error dynamics and its convergence are provided.

KEYWORDS: Flexible joint robot; hysteresis; joint torsion; robot control; virtual torsion sensor; dissipativity.

1. INTRODUCTION

The analysis, modeling and control of robotic manipulators with flexible joints have been and remain challenging topics in both theory and practice, see e.g. refs. [13, 14, 32] and [1, 8, 16]. Recent trends towards more lightweight and flexible structures underpin the importance of flexible joints in the robotics. Among the related issues are the sensor reduction and, at the same time, the enhanced accuracy required from positioning of the robotic end-tools and, correspondingly, single actuated joints with gearing.

An inherent problem with elasticities in robotic joints is that they are mostly nonlinear as for torque-torsion characteristics, and even subject to certain state memory owing to internal friction, structural damping, mechanical losses and other hidden effects. Note that the impact of linear joint elasticities on the robot modeling and regulation has been widely addressed in the control design literature e.g. refs. [13, 15, 32, 35]. It has been initially discussed in terms of positioning in ref. [35] and, later on, trajectory tracking in ref. [5]. The latter elaborated on how the desired motor trajectory can be obtained from that of the joint link, when accounting explicitly for the linear joint elasticities. Several works, see refs. [10, 18, 34], have also been concerned with the analysis and modeling of nonlinear, correspondingly hysteretic, behavior of the joint transmissions, particularly those incorporating harmonic drive gearing. However, to date, hysteresis-related problems in elastic robotic joints have not yet been efficiently resolved, in terms of a precise control of the joint loads. It is particularly relevant when only the motor-side sensing (i.e. encoder) is available for the motion control. Further it should be noted that,

---

* Corresponding author. E-mail: michael.ruderman@uia.no

until now, not many robot manipulators have been equipped with embedded link- or load-side sensing. Remarkable is that issues related to nonlinear torsion-torque characteristics have also been acknowledged for that type of manipulators, e.g. ref. [37].

Apparently, hysteresis-type nonlinearities in the flexible robotic joints provide remarkable challenges for analysis of dynamics and control design. This is, above all, due to the cumbersome proof of the closed-loop stability and nontrivial trajectory solutions. Few studies with application examples can be found in the literature, dealing with analysis of the system dynamics which incorporates hysteresis in feedback. When treating the stability of nonlinear feedback systems, most developments assume a memoryless nonlinearity; see previous studies in refs. [4, 12] and seminal literature, e.g., [17]. At the same time, some fundamental properties of nonlinear feedback systems with memory lead back to early work [2]. In ref. [11], the control stability of a dynamic system with hysteresis in feedback is also analyzed, based on the passivity approach. However, it is not the hysteresis output but its time derivative that has been considered in the feedback. More recent work, see ref. [21], has analyzed the absolute stability of linear systems with hysteresis feedback. There, the hysteresis nonlinearity was requested to be a Duhem operator, see ref. [19] for detail, and the reported examples were restricted to the second-order dynamic systems.

The aim of this paper is to analyze and prove the stability of incorporating VTS in the control loop of a flexible joint manipulator, and that with hysteresis in torsion-torque characteristics. We recall that VTS has been proposed and elaborated in refs. [22, 24–26], also with experimental results related to a single joint with harmonic drive type gearing. Despite the VTS arises as a suitable approach, as evaluated both in numerical simulations and experiments, the previously addressed stability of VTS inclusion relies solely on mild assumptions about the inherently dissipative nature of hysteresis and associated damping. The present work is partially based on preliminary results of the stability analysis presented in ref. [23] albeit for static nonlinear stiffness without memory, i.e., without hysteresis. The recent study considers the dissipative joint behavior in relation to hysteresis, while developing an absolute stability analysis based on the Popov criteria, including sector conditions.

In what follows, the problem of VTS inclusion into control of the flexible robot joints is formulated in sections 2 and 3. First, we summarize the modeling assumptions and control of flexible robot joints. Then, we introduce the problem of VTS inclusion into the position feedback loop. The main results are given in sections 4 and 5. In section 4, we discuss the dissipativity and passivity of the torsion-torque hysteresis map, with a detailed analysis of two boundary cases of zero and maximal energy dissipations within one cycle. The absolute stability of VTS inclusion in the control is discussed in section 5 together with illustrative numerical examples. Brief conclusions are given in section 6.

2. MODELING AND CONTROL OF FLEXIBLE ROBOT JOINTS

Considering the vectors of motor coordinates $\theta \in \mathbb{R}^n$, link coordinates $q \in \mathbb{R}^n$, and relative displacements between the both $x = \theta - q$, the dynamics of an n-joints robotic manipulator with joint elasticities can be written as below. Note that the nominal gear ratio is assumed to be already incorporated into the joint coordinates, correspondingly forces and, therefore, omitted in the following for the sake of simplicity.

$$H\ddot{q} + \Phi(q, t) = h(x) + D\dot{x}, \tag{1}$$

$$J\ddot{\theta} + h(x) + D\dot{x} = u(t) - f(t). \tag{2}$$

Here, the lumped link and motor inertias are denoted by H and J matrices, respectively, while the link inertias are assumed to be already decoupled from the configuration-dependent inertial terms, see e.g. Chapter 6 in ref. [29]. That means the overall state-dependent inertia matrix (like it is typically used in robotics literature) can been written as a superposition $\tilde{H}(q) = H + \hat{H}(q)$, cf. with ref. [33]. Following to that, the

configuration-dependent inertial elements $\hat{H}$ are collected together with all residual coupling effects, i.e., Coriolis-centrifugal and gravity torques, in a generalized nonlinear function $\Phi(\cdot)$. Here, the functional dependency on the derivatives of q, i.e. angular velocities and accelerations, are implicitly included. It is equally assumed that Φ can be decoupled, or at least minimized, by the applied model-based control, either in a feedback linearization manner, or by a torque feedforwarding; see e.g. refs. [30, 33] for detail. The transmitted torque, and in turn the reactive joint torque, are calculated as

$$\tau = h(x) + D\dot{x}, \tag{3}$$

where the rate-independent nonlinear stiffness map is h and the viscous damping coefficient is D. The overall motor friction

$$f = B\dot{\theta} + \beta(\dot{\theta}) \tag{4}$$

is assumed to be a superposition of the viscous term with B-coefficient, which is the linear damping, and the nonlinear friction term β. The latter is understood as dissipative (see e.g. refs. [27, 28]) and amplitude-bounded, similar to the Coulomb friction during a unidirectional motion. Note that f is assumed to be known at the stage of designing and applying the VTS. During analysis of VTS inclusion, as presented in Section 5, the friction f can be deliberately neglected for the sake of simplicity. This is valid since it acts as an additional motor-side damping and is largely compensated together with Φ. Furthermore, we note that $f = 0$ would deal with a rather underdamped 'worst case' when analyzing the closed-loop stability of the controlled system.

For a possibly fast dynamic response of the controlled robotic manipulator, model-based torque feedforwarding is a common practice; see, e.g., [30, 33] for detail. It means that, given the reference joint trajectory $\theta_r(t) \in \mathcal{C}^2$, the centralized model of manipulator dynamics computes the required motor torques u_{ff}, which are directly applied to the system (1)), (2). Note that the reference trajectory should be at least twice continuously differentiable, so as to allow for resolving the rigid inverse dynamics, which includes the acceleration-dependent terms. This requirement is general one for the rigid robotic manipulators, and can be seen as a minimum requirement in case of the flexible joint manipulators. In order to avoid jerks and reduce excitation of the transient joint oscillations, the reference trajectory can be further requested to have a higher order of continuity, meaning $\mathcal{C}^3$ or $\mathcal{C}^4$. It is also worth noting that a model-based torque feedforwarding mostly relies on the assumed rigid manipulator dynamics, so that no explicit joint elasticities, as those in (1), (2), are taken into account when computing $u_{ff}(\theta_r(t))$. This simplification is mostly due to complexity of the inverse dynamic model with high-order derivatives of the states and state-dependent matrices. Recall that the latter should be resolved in real time. Yet, the full-order dynamics' inverse feedforwarding can be found in the literature, – for linear joint stiffness in ref. [6] and for nonlinear joint stiffness with hysteresis in ref. [22].

By assuming the inevitable modeling errors and system uncertainties in (1), (2), the residual control error $e = \theta_r - \theta$ can be (traditionally) minimized by the proportional-derivative feedback action. Following to that, the total control vector results in

$$u = u_{ff} + K_p e + K_d \dot{e}. \tag{5}$$

Note that the feedback control gains $K_p, K_d > 0$ allow for a robust and design-specific shaping of the error dynamics, in terms of the bandwidth and damping ratio.

The residual error dynamics of the system (1), (2), with the control law (5), can be written as

$$\tilde{H}(q)\ddot{q} - h(x) - D\dot{x} = 0, \tag{6}$$

$$J\ddot{e} + (D + K_d)\dot{e} + K_p e - h(x) + D\dot{q} = 0. \tag{7}$$

Note that we skip any further explicit consideration of the feedforward control part

$$u_{ff} = \hat{J}\ddot{\theta}_r + \hat{f}(\dot{\theta}_r) + \hat{D}\dot{\theta}_r + \hat{\Phi}(\theta_r, t). \tag{8}$$

which is to compensate for both modeled (denoted by variables with 'hat') nonlinearities like the motor friction and configuration-dependent manipulator dynamics. Following assumptions and simplification justify the use of feedforward control (8). Since the friction disturbance (4) is the matched one with control input, the feedforward compensation of f-term implies directly. The Φ-term, containing the configuration-dependent dynamics of the rigid manipulator, can be captured under mild assumptions with the motor-side arguments i.e. $\theta \approx q$, $\dot{\theta} \approx \dot{q}$. Note that this holds once the relative displacement x is bounded and relatively low, compared to the motor and link displacements, while the transients of $\dot{x}$ are sufficiently damped by the joint structure. Further, one can notice that (6) still confronts the configuration-dependent inertia matrix $\tilde{H}$, so that the residual control errors will excite the controlled motion dynamics – an effect which cannot be compensated via feedforwarding. Since the configuration-dependent inertia matrix of manipulator is upper- and lower-bounded (see e.g. refs. [30,33] for detail), one can assume and write $H_{\min} \leq \tilde{H}(q) \leq H_{\max}$ which is sufficient for analysis. Note that here and further on, the dynamics (6), (7) will be interpreted as a single-input-single-output (SISO) system by considering any single, decoupled by means of u_{ff}, robotic joint with the upper and lower boundaries of inertia, as introduced above.

3. VIRTUAL TORSION SENSOR

Aim of the VTS, as it was introduced and elaborated for application in the control, see refs. [22, 24, 26], is to predict the relative joint torsion by means of the estimated reactive joint torque which is subsequently mapped via an inverse torsion-torque function. The latter can be considered either as linear or nonlinear, equally as incorporating hysteresis memory in the general case that we will assume below. Independently on the underlying model, the inverse hysteresis map should be deterministic for the given initial state and input series, and computable in the real time. Simple yet robust estimation of the reactive joint torque bases on the approach known as generalized momenta, see refs. [7,9] for detail. In the following, we denote the observed (i.e. estimated) reactive joint torque by r which follows the stable first-order dynamics

$$\dot{r} + Lr = L\tau. \tag{9}$$

Note that the VTS ensures an exponential convergence of r to the τ value, while the latter is the unknown reactive joint torque (5) which should be observed. For more details on VTS and its properties we refer to [22, 24, 26].

The observed reactive joint torque serves as the input of inverse torsion-torque map. It is worth noting that due to relatively fast transients of the torque dynamics (this due to high joint stiffness) compared to the observer time constant L^{-1}, and the unavailable $\dot{x}$ state, the viscous damping term is excluded, cf. with (3). This is justified as the viscous term provides an additional damping and, therefore, its exclusion constitutes rather a worst case for stability analysis. Once the nonlinear rate-independent map $\tau = h(x)$ is given, the joint torsion predicted by VTS results in

$$\tilde{x} \approx h^{-1}(r). \tag{10}$$

Here we note that an appropriate L-gain provides a low-pass filtering of the damping-related torque components, so that the estimation error is $(h(x) - r) \to -\infty$ dB at low frequencies, and $(h(x) - r) \to 0$ dB at higher frequencies. At the same time, the amplitude of $h(x)$ functional is constant for all frequencies and relatively high, due to the high joint stiffness.

The problem of including VTS into a feedback control loop is given as follows and schematically illustrated in Fig. 1. Two concentrated inertias represent the motor and
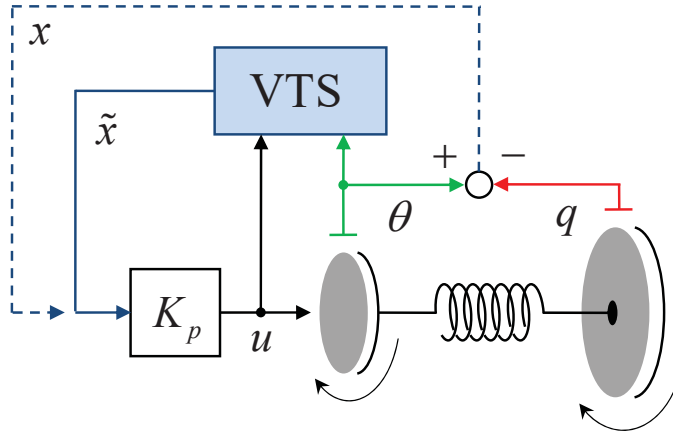

Fig. 1. Flexible robotic joint with direct and VTS-based torsion feedback.

link sides connected by a (nonlinear) spring, which imitates the flexible joint, cf. (1), (2). Recall that the configuration-dependent link inertia is assumed to be decoupled, e.g., by the feedforward torque control, see Section 2. The differential angular displacement x between the motor and link axes, which we will further denote as *joint torsion*, deteriorates the motion control of the link. Due to a finite stiffness, it produces the disturbing vibrations at the resonance frequency at each transient phase of the motion response. Moreover, it distorts the steady-state accuracy of the link position at nonzero equilibrium torque, for instance, due to the gravity or external forces acting on the manipulator. Recall that since the robotic manipulator is expected to drive, correspondingly to position, a payload attached to the end-effector, the control accuracy in the link space $\{q\}$ is of our primary interest. It is apparent that attenuation of the transient and steady-state link errors requires, to some extent, the information to be available about the link position, that means equally about the torsion. Here, we should stress again that, nowadays, the industrial robots are mostly equipped with motor-side encoders only. Once available, the torsion quantity can be incorporated into the motor control loop, thus providing an "offset" to the motor feedback position and, in this way, achieving a better position accuracy in the $\{q\}$-space. Moreover, using if available the differential velocity $\dot{x}$ in feedback loop can also reduce the disturbing link oscillations, as shown e.g. in ref. [13].

The VTS predicts the relative joint torsion $\tilde{x}$ by using the available motor torque u and velocity $\dot{\theta}$, both of which are the process quantities. Since the relative joint torsion is used to augment the feedback motor position under control and, therefore, to account for differences between the joint input and output displacement, the proportional gain K_p of motor controller has to be considered. The feedback motor control is assumed as already designed and robust, in terms of the amplitude and phase margins and disturbance attenuation. The question that arises now is concerned with how stable the feedback of relative joint torsion is. It can be investigated independently of the designed motor control, since only the proportional feedback of the joint torsion is used. This case, the feedback control (5), here without feedforward part, is substituted by

$$u^* = K_p e + K_d \dot{e} + K_p \tilde{x}, \tag{11}$$

where the last term is VTS predicted, cf. (9), (10). Therefore, the torsion feedback appears as an inner control loop nested inside of the overall cascaded control structure. Apart from a general question about the torsion feedback stability, an inclusion of VTS-based estimate instead of the real measured torsion requires a more detailed analysis. Note that

the absolute stability of VTS inclusion for the nonlinear but memoryless (i.e. without hysteresis) joint stiffness has been preliminary shown in ref. [23].

4. DISSIPATIVE HYSTERESIS TORQUE MAP

We first consider a generalized torsion-torque hysteresis map $\tau = h(x)$ with two necessary requirements – to be (i) rate-independent, see e.g. ref. [3], and (ii) clockwise in the input-output (I/O) sense. The first one means that the output trajectories, and in turn energy conservation or dissipation per cycle, do not depend on the input rate. Therefore, the $h(\cdot)$-map is invariant in relation to the affine transformations of time, i.e., $a + bt \ \forall \ a \in \mathbb{R}, \ b \in \mathbb{R}^+$. The second requirement implies that for any pair of two output trajectory segments, which are connected via the input reversal point, it is valid for the forward segment, for which $\dot{x} > 0$, to lie always above the backward segment, for which $\dot{x} < 0$. This type of nonlinear spring behavior can be directly incorporated into the stiffness model. In the structural mechanics, it is often referred to as hysteresis damping or structural damping.

4.1. Energy dissipation and lost motion

Since the torsion-torque map characterizes a spring element, the corresponding energy storage can be considered for any two points $x_2 > x_1$. Without loss of generality, we assume the pair of input states to be (x_1, x_2), as exemplary depicted in Fig. 2, in which x_1 represents an arbitrary initial state and x_2 represents the next reversal state of the input sequence. It is evident that the total energy of spring can be written as

$$E(t) = \int\limits_{X(t)} h(\sigma)\mathrm{d}\sigma + E(0), \tag{12}$$

where $X(t)$ is the entire input trajectory with $X(0) = x_0$. For simplicity, we assume zero initial energy storage $E(0) = 0$. It is worth emphasizing that here no kinetic energy has to be taken into account since the torsion-torque map is rate-independent. Thus the overall torque (or generalized force) evolution does not depend on $|\dot{x}|$ but only on $\mathrm{sign}(\dot{x})$.
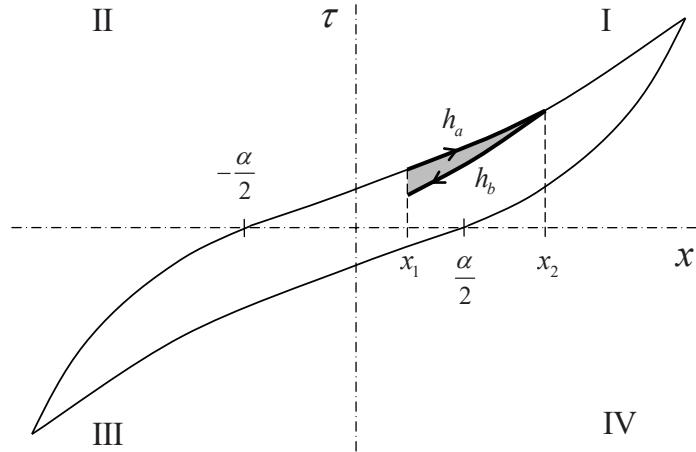

Fig. 2. Torsion-torque h-hysteresis loop with input reversal.

Coming back to the $[x_1, x_2]$ interval, it can be seen that the overall change in the energy level between both states is given by

$$E(x_2) - E(x_1) = \int\limits_{x_1}^{x_2} h(x)\mathrm{d}x. \tag{13}$$

If the nonlinear torsion-torque map is first assumed to be non-hysteretic, then the forward and backward segments of the output trajectory coincide with each other, so that

$$\Delta E_{2-1} = \int_{x_1}^{x_2} h_a(x)\mathrm{d}x = -\int_{x_2}^{x_1} h_a(x)\mathrm{d}x, \tag{14}$$

$$\Delta E_{1-2} = \int_{x_2}^{x_1} h_a(x)\mathrm{d}x = -\int_{x_1}^{x_2} h_a(x)\mathrm{d}x. \tag{15}$$

Apparently, the total energy change during one x_1-x_2-x_1 cycle is $\Delta E_{2-1} + \Delta E_{1-2} = 0$, meaning that the nonlinear spring behaves as lossless. That is, the total potential energy stored in the rotary spring during relative torsion can be recuperated after twisting back. Apparently, there is no damping captured by the $h(\cdot)$ function without hysteresis.

Next, when considering the actual hysteresis branching after input reversal, one can show that the total energy change is

$$\Delta E = \Delta E_{2-1} + \Delta E_{1-2} = \int_{x_1}^{x_2} h_a(x)\mathrm{d}x - \int_{x_1}^{x_2} h_b(x)\mathrm{d}x \neq 0.$$

Since the first summand constitutes the potential energy which has been stored when moving from x_1 to x_2, and the second summand corresponds to the potential energy which has been released on the way back, their positive difference $\Delta E > 0$ represents the total energy losses during one x_1-x_2-x_1 cycle. It can be seen that this corresponds to the area of hysteresis loop, which is gray-shaded in Fig. 2. Note that the loop should not be necessarily closed, and the corresponding area reflects the instantaneous energy losses after an arbitrary input reversal. Wider hysteresis loops represent larger hysteresis damping, while the closed loop area and the shape of hysteresis branches can vary, depending on the input amplitude and its history.

The temporal change in the system energy can be analyzed by taking the time derivative of (12) that results in

$$\dot{E}(t) = \frac{\mathrm{d}}{\mathrm{d}t}\int h(x)\mathrm{d}x = h(x)\dot{x}. \tag{16}$$

One can see that the energy rate is proportional to that of the input, i.e. $\dot{x}$, on the basis that the latter drives the output state according to $h(x)$. Since $h(\cdot)$ is rate-independent (in other words a static but, at the same time, multivalued mapping), it is of interest to make a qualitative comparison of the energy changes, depending on the sign of both the hysteresis output and input rate. Here, some $|\dot{x}| = \mathrm{const}$ can be assumed. From (16), it becomes apparent that $\dot{E} > 0 \,\forall\, \dot{x} > 0$ in Quadrant I, while $\dot{E} > 0 \,\forall\, \dot{x} < 0$ in Quadrant III of the I/O plane, cf. Fig. 2. That means that independently of the hysteresis damping, the nonlinear spring behaves conventionally in Quadrants I and III, i.e., by increasing the potential energy during the elongation for $x > 0$ and during compression for $x < 0$. Note that when $x = 0$, the spring is neither elongated nor compressed, while $h(0) \neq 0$ represents the residual stress manifesting the hysteresis. On the contrary, Quadrants II and IV can be seen as a 'reversal' spring, since here the input displacement and output force have opposite signs. However, the sign of energy changes holds according to (16). That means the Quadrants I and II form a half-plane where $\dot{x} > 0$ implies $\dot{E} > 0$. Correspondingly, Quadrants III and IV form the complementary half-plane, where $\dot{x} < 0$ implies $\dot{E} > 0$. Note that the above distinction between the Quadrants I-IV of I/O map does not violate the energy dissipation and therefore hysteresis damping at any reversal cycle. At the same time, it creates an effect which is similar in appearance to a quasi-plasticity, i.e., with residual torques at zero displacement. In structural

mechanics, this is commonly known as the Bauschinger effect, which is defined by the so-called kinematic/isotropic hardening occurring at the cyclic loading, or deformation, and manifesting hysteresis in the stress-strain curves. Note that for moderate strains and cyclic loading, the cyclic hardening/softening provides a hysteresis loop stabilization. Therefore, a plastic fraction of the total strain can be assumed as relatively low as well as with constant boundary for the bounded stress. In terms of the torsion-torque hysteresis, a constant value, i.e.

$$\max h^{-1}(0) - \min h^{-1}(0) := \alpha \tag{17}$$

can be therefore assigned, which we will denote as the *band* of hysteresis lost motion. Note that for symmetric hysteresis springs, the band is symmetrical to the origin, so that the 'quasi-plastic' (residual) deformation is bounded by $[-\alpha/2, \alpha/2]$. Here, we deliberately use the term 'quasi-plastic', since a complex mechanical assembly of the flexible joint is only approximated by a nonlinear hysteresis spring. In fact, it contains a number of solid elements in contact with each other which feature a specific geometry and stiffness. Hence, the clearances between the elements and internal frictional interactions contribute to such 'spurious' plastic appearance in the I/O mapping.

4.2. Hysteresis spring as dissipative operator
In the previous section, we showed that the hysteresis map $\tau = h(x)$ dissipates energy at each input reversal. Below, we make use of the concept of system dissipativity, or passivity, which has been established as particularly suitable for nonlinear system analysis and control, see e.g. refs. [17,20], while introduced in ref. [36]. For a static I/O map, with the input u and output y representing an "energy pair" of the physical system, a direct sector test (see ref. [17] for details) provides sufficient proof as to whether the system is passive. If, for any u-value, $yu \geq 0$, then the energy consumption is positive and the system is passive. In other words, the I/O graph should only lie in the Quadrants I and III. Since the static hysteresis map is not memoryless, cf. ref. [17], but represents a multi-valued function lying in all four quadrants and continuously increasing, the direct sector test does not allow for a straightforward conclusion concerning passivity. Thus, we need to take special measures, similar as it is required in case of passivity analysis of dynamic nonlinear systems. Following ref. [4], a system with the state $z \in Z$ is passive if it is dissipative with the supply rate $w = \langle y, u \rangle$ and nonnegative storage function $V : Z \to \mathbb{R}$ with $V(0) = 0$, so that

$$V(z) - V(z_0) \leq \int_0^t yu \, \mathrm{d}t. \tag{18}$$

Note that $V(z)$ is a Lyapunov function candidate representing the energy level of the system as function of the state. Assuming the storage function is continuously differentiable (with respect to the time) results in the systems' passive condition if

$$\dot{V}(z) \leq yu, \tag{19}$$

independently of the initial state z_0. Apparently, the system is lossless when $\dot{V} = yu$.

Considering the hysteresis map introduced in Section 4.1, with a state given by the hysteresis output, i.e., $y = \tau$, we assume the storage function as follows:

$$V = \eta \frac{1}{2} \tau^2 - \int_\Gamma h(x) \mathrm{d}x. \tag{20}$$

Note that Γ is the path traversed in the (x, τ) plane. We also note that the first summand in (20) constitutes the potential energy of the spring, while, in the case of a linear stiffness, it is valid $\eta = k^{-1}$ for a positive spring constant k. The path integral captures the amount

of dissipated energy once the input direction changes. Regardless of whether operation takes place in the upper or lower half-plane, i.e. for $\tau > 0$ or $\tau < 0$, respectively, one can see that for a certain $\eta > 0$, the first summand in (20) remains always larger than the second one. Therefore V remains nonnegative for all (x, τ) trajectories. Note that (20) belongs to a certain class of the Lyapunov functionals, as introduced in ref. [2].

For the given I/O system, we assume the supply rate to be

$$w(y, u) = \tau x, \tag{21}$$

while substituting it with time derivative of (20) into (19), one obtains

$$\eta \tau \dot{\tau} - \tau \dot{x} \leq \tau x. \tag{22}$$

Further substituting τ and $\dot{\tau}$ by the hysteresis map, and its time derivative, results in

$$h(x)\Big(\eta \frac{\partial h}{\partial x} - 1\Big)\dot{x} \leq h(x)x. \tag{23}$$

It appears that the proof (23) inequality requires the case difference for all four quadrants, equally as for each of the positive and negative input velocities. This could render our analysis to be too cumbersome and impractical in terms of incorporating hysteresis into the overall system dynamics. Instead, we will consider two boundary cases for hysteresis $h(\cdot)$, which satisfy the dissipation property addressed in Section 4.1. Afterwards we will assume that all other shapes of a clockwise hysteresis are lying within these boundary conditions.

First, we consider the upper boundary of maximal energy dissipation at each reversal, and consistently assume the related hysteresis map to be

$$\tau = \bar{h}(x) = kx + c\,\mathrm{sign}(\dot{x}). \tag{24}$$

Note that (24) remains rate-independent, since the sign of input velocity solely captures the directional changes without any input or output dynamics. One can recognize that (24) represents a case in which the linear spring is combined with Coulomb-type friction, so that the amount of energy dissipated between two consecutive points $x_2 > x_1$ is

$$E_h = \int_{x_1}^{x_2} c\,\mathrm{sign}(\dot{x})\mathrm{d}x = c\,\mathrm{sign}(\dot{x})(x_2 - x_1). \tag{25}$$

Therefore, the damping rate is velocity-independent; moreover it is constant for any path Γ traversed in the (x, τ) plane, cf. (20). The torsion-torque hysteresis loop parameterized by $c, k > 0$ is shown in Fig. 3 with three exemplary reversal points. Note that the hysteresis loop is clockwise, and the stepwise transitions between the upper and lower slopes, $kx + c$ and $kx - c$, respectively, provide the maximal possible energy dissipation at each reversal cycle. Here, the time derivative of the storage function (20) results in

$$\dot{V} = kx\dot{x} - \tau\dot{x} = -c|\dot{x}|, \tag{26}$$

from which one can see that the system behaves as lossless only at zero velocity. Otherwise, any input changes provoke energy dissipation with the rate proportional to the magnitude of input velocity. One can recognize that the system is dissipative, while its passivity should first be investigated, based on (21), (22). Substituting (26) and (24) into (22) results in

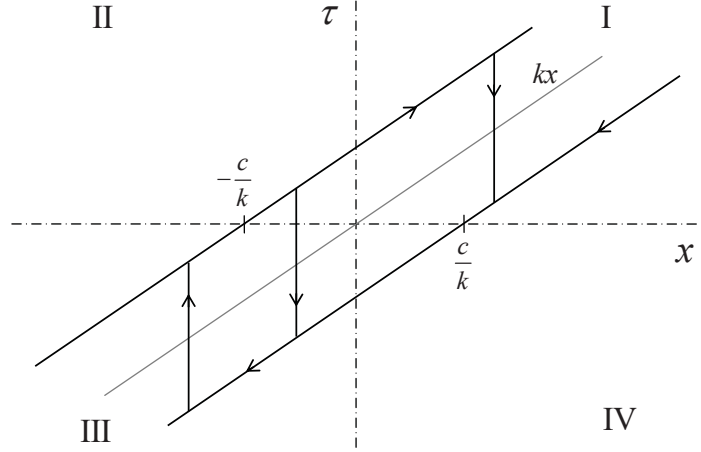$$-c\,|\dot{x}| \leq x\big(kx + c\,\mathrm{sign}(\dot{x})\big). \tag{27}$$

Fig. 3. Torsion-torque $\bar{h}$-hysteresis loop with input reversals.

From the associated case difference, and that for the positive and negative input values, one can see that in order to ensure (27) holds, two conditions should be fulfilled

$$x \geq \frac{c}{k} \quad \text{if } x > 0 \wedge \dot{x} < 0, \tag{28}$$

$$x \leq -\frac{c}{k} \quad \text{if } x < 0 \wedge \dot{x} > 0. \tag{29}$$

From (28), (29), one can conclude that the hysteresis map (24) is almost always passive, except for a decreasing trajectory within Quadrant IV and an increasing trajectory within Quadrant II. Note that if, in one of both cases, the input direction changes, the output immediately jumps into the sector of system passivity, i.e. into Quadrant I or III, respectively. Also note that the threshold values in (28), (29) correspond to the band of hysteresis lost motion, cf. (17), so that $c/k = 1/2\alpha$. However, unlike in the case of piecewise continuous hysteresis map $h(\cdot)$, the input range $[-c/k, c/k]$ cannot be directly interpreted as a quasi-plastic residual deformation, since the output torque always belongs to one of the three manifolds, $\{kx - c, kx, kx + c\}$, while only the discrete (stepwise) transitions in between are possible.

Since the lower boundary case assumes no energy dissipation at the input reversals, the same lines of argument as above can be pursued, while assuming $c = 0$. In this case, the hysteresis in Fig. 3 'collapses' into a linear stiffness slope $\tau = \underline{h} = kx$, thus representing a classical spring without energy losses. Substituting $c = 0$ into (27) results in

$$0 \leq kx^2.$$

That means the system is always passive, equally as lossless, since $\dot{V} = \tau x$. Here, we are reminded that, if the torsion-torque map is an arbitrary static memoryless function, i.e., without hysteresis, its passivity can be directly proven by the sector condition $\underline{h}(x)x \geq 0$, cf. with ref. [17]. Therefore, no explicit analysis as above is required. The absolute stability of the torsion feedback with nonlinear memoryless stiffness given, for example, by the cubic polynomial function has been demonstrated in ref. [23] for both, direct measurement and VTS-prediction. In that case, the well-known Popov criterion (see e.g. [31] for detail) has been applied. In the next section, we briefly review the results from ref. [23], before considering the case of a hysteresis map h.

5. STABILITY OF VTS INCLUSION

5.1. Nonlinear memoryless stiffness
In order to analyze VTS inclusion into the closed loop, the control (11) should be accordingly incorporated. Following to that, $K_p\tilde{x}$ appears on the right-hand side of the error dynamics (7). Since the torsion-torque map is static and the joint torque estimation is driven by (9), it can be assumed that the dynamic relationship between the joint torsion and its estimate is given by

$$L^{-1}\dot{\tilde{x}} + \tilde{x} = x. \tag{30}$$

Note that while certain steady-state errors between x and $\tilde{x}$ are possible, caused by the mapping errors of $h(\cdot)$, the first-order time delay behavior (30) always remains valid due to observer dynamics (9), which is governed by the design parameter L. The control error dynamics (6), (7), modified by the VTS inclusion as above, has one static nonlinearity in feedback, so that the overall system can be written in the state-space form

$$\dot{\mathbf{x}} = \mathbf{A}\mathbf{x} - \mathbf{b}\gamma(y), \quad y = \mathbf{c}^T\mathbf{x}. \tag{31}$$

The state vector is $\mathbf{x} = [q, \dot{q}, \theta, \dot{\theta}, \tilde{x}]$. For more details on the state-space model i.e. their matrices $\mathbf{A}$, $\mathbf{b}$, and $\mathbf{c}$ see ref. [23]. The above form is suitable for the absolute stability analysis by means of the well-known Popov criteria; for detail see e.g. ref. [31]. One can decompose the overall torsion-torque map in such a way that the linear stiffness component is in superposition with the nonlinear one

$$h(y) = ky + \gamma(y). \tag{32}$$

While the residual control error has been considered in (7), the above state-space model is equivalent to that when assuming a zero reference value and $e(0) \neq 0$. One can show that the system matrix $\mathbf{A}$ is Hurwitz, and the pair $[\mathbf{A}, \mathbf{b}]$ is controllable. Thus, the first Popov criterion is already fulfilled.

The second condition concerns the static nonlinearity in feedback, which has to comply with sector criterion, see ref. [17] for detail,

$$\forall y \neq 0 \ \Rightarrow \ k_1 \leq \frac{\gamma(y)}{y} \leq k_2, \tag{33}$$

for two nonnegative numbers k_1 and k_2. Recall that the passivity sector condition, cf. Section 4.2, allows for the above sector to be restricted to $[0, k_2]$, so that the Popov criterion is applicable here instead of a more general circle criterion. The latter also allows for $k_1 < 0$. In ref. [23], it has been shown that for a bounded joint torsion, that is inherent for real mechanical structures, the cubic polynomial nonlinearity belongs locally to the sector $[0, k_2]$ for some $x_{\min} \leq x \leq x_{\max}$, and that the Popov criterion is directly applicable.

The third condition of the Popov criterion of absolute stability requires that, for the transfer function

$$G(s) = \mathbf{c}^T(s\mathbf{I} - \mathbf{A})^{-1}\mathbf{b},$$

there exists a strictly positive number σ, whereby

$$\forall \omega \geq 0 \quad \mathrm{Re}\big[(1 + j\sigma\omega)G(j\omega)\big] + \frac{1}{k_2} \geq \varepsilon, \tag{34}$$

for any arbitrary $\varepsilon > 0$. The third condition is much easier to interpret by using the so-called Popov plot, which visualizes the polar plot $\omega\,\mathrm{Im}\{G(j\omega)\}$ over $\mathrm{Re}\{G(j\omega)\}$ for

the frequencies starting from $\omega \to 0$ and going towards $\omega \to \infty$. In turn, one can prove whether a strictly positive σ exists for a sufficiently large k_2, so that the $1/\sigma$ slope, which goes through $-1/k_2$, does not intersect the polar plot.

5.2. *Nonlinear stiffness with hysteresis*

In order to prove the stability of system (31) for the case of feedback nonlinearity with hysteresis, one can make use of the passivity theorem, which states that the feedback connection of two passive systems is passive. This implies stability of the closed loop. However, this generally established approach bears the challenge of showing the passivity of the dynamic linear subsystem, which, in turn, requires the evaluation of the positive realness of the transfer function $G(s)$. The latter can be achieved by using the well-known positive real lemma, known as the Kalman-Yakubovich-Popov lemma; see e.g. ref. [17] for detail. The proof of existence for the required matrices satisfying the lemma's equalities can present an obstacle in view of the 5×5 system matrix. Therefore, we pursue an alternative strategy which, again, relies on the Popov criteria of absolute stability. The elegance of the proposed method becomes evident in light of the corresponding nonlinearity decomposition and the related approach of loop transformations.

Assume that the feedback nonlinearity now takes the form

$$h(y) = ky + \gamma(y) + \delta(\dot{y}), \quad \text{with} \quad \delta = c\,\mathrm{sign}(\dot{y}), \tag{35}$$

cf. (24) and (32). Apparently, incorporating the velocity sign extends the case we analyzed in Section 5.1 to the upper-boundary case of hysteresis, cf. Section 4.2. Since the linear stiffness k is already accumulated in the system matrix $\mathbf{A}$, and both nonlinear terms in (35) are in superposition to each other, two separated nonlinearity loops can be considered. For the first one, the linear dynamics is $G(s)$, while for the second one, it is $G(s)s$. Therefore, the system (31), (35) can be transformed into that depicted in Fig. 4.
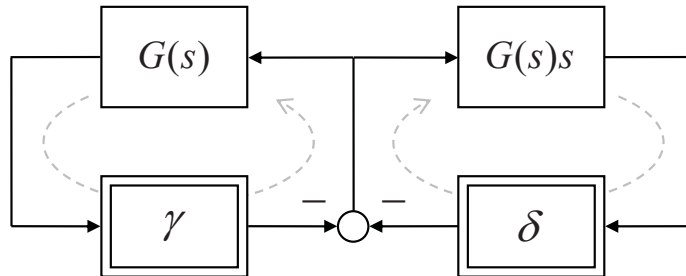

Fig. 4. Transformed loop with two feedback nonlinearities.

It is apparent that the output of each nonlinearity enters into the opposite loop as an exogenous input, thus without influencing its eigen-behavior. While the absolute stability of the $\gamma\,G(s)$ closed-loop has been proven in Section 5.1, the same procedure can be made for the $\delta G(s)s$ closed-loop as follows.

One can show that the system matrix of the extended transfer function $G(s)s$ remains Hurwitz, while the new pair $[\mathbf{A}^*, \mathbf{b}^*]$ of the corresponding state-space model is controllable as well. By inspecting the $\delta(\cdot)$-nonlinearity, one can see that it belongs to the sector $[0, \infty]$, so that $1/k_2 \to 0$. Note that here the k_2-value is not necessarily the same as in the case of γ-nonlinearity. Evaluating (34) shows that the Popov plot for $G(j\omega)j\omega$ always lies in the right half-plane, while it goes towards 0 for $\omega \to 0$ and towards some negative value on the imaginary axis for $\omega \to \infty$. Since this constitutes the upper boundary of h-discontinuity at x-reversals, it is apparent that any piecewise continuous hysteresis branches, after the sign of $\dot{x}$ changes, will lead to $k_2 < \infty$. Therefore, $-1/k_2$ always lies to the left of the origin of the Popov plot, even if infinitesimally close to zero from the left. For this locus, one can always find a strictly positive σ, so that the $1/\sigma$
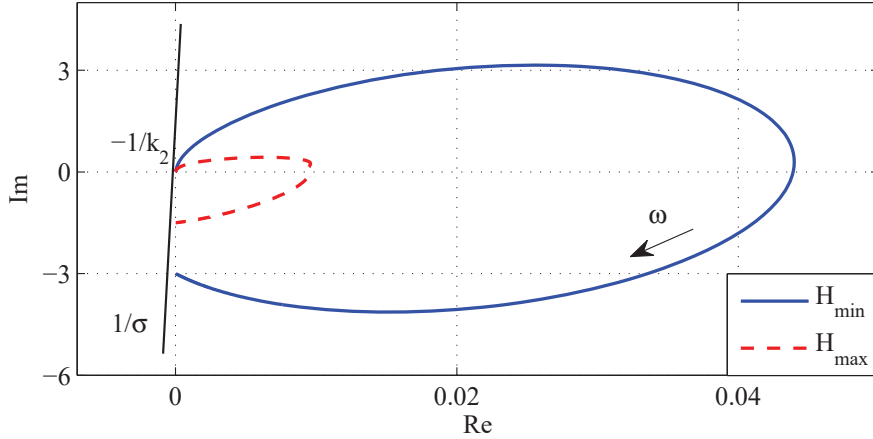
Fig. 5. Popov plots of system $G(s)s$ with feedback nonlinearity $c\,\mathrm{sign}(\dot{y})$.

slope does not intersect the polar plot. This implies that the third condition of Popov criterion is fulfilled. By implication, the $\delta\,G(s)s$ loop is equally stable. An example of the Popov plot, and that for the values assumed further in Table I, is shown in Fig. 5.

5.3. Numerical example

In the following, a numerical example of the closed-loop behavior of system (6), (7), with the VTS-based torsion feedback, meaning $K_p\tilde{x}$ on the right-hand side of (7), is shown. The torsion-torque map is assumed to be once according to (32) and once according to (35). The nonlinear static map is described by the cubic polynomial function $\gamma(y) = py^3$, and the link inertia is set to its upper bound $H_{\max}$. The VTS is implemented according to Section 3, while β is assumed to be zero for the sake of simplicity. All parameters used in the numerical setup are listed in Table I. For sufficiently exciting the transient joint oscillations, the stepwise conditions are realized by assuming $0.2x(\infty) \approx e(0) \neq 0$. Note that all parameters are assigned without giving explicit physical units, so that the unitless motion states can be demonstrated. This allows for an arbitrary system scaling, while the time argument is conventionally kept in seconds. To allow for a sufficiently visible joint torque, correspondingly torsion, under in the steady-state, the case of a gravity load is additionally demonstrated. For that purposed, the left-hand side of (6) is

Table I . Parameters of numerical simulation..

Param.	Value	Param.	Value	Param.	Value	Param.	Value
J	1	D	5	K_p	10000	g	2000
$H_{\min}$	0.5	k	10000	K_d	200	c	1000
$H_{\max}$	2	p	10000	L	10	$e(0)$	1

modified by adding a positive g-term, which summarizes the gravity constant, mass and lever arm of the link. Note that the gravity torque can be approximated as constant for the small displacements e around an equilibrium point. We recall that nonzero gravity provokes both the transient and steady-state deflections of a flexible joint and, thus, end-position errors of the robot link.

The time response of the e and q trajectories are show in Fig. 6. Recall that for zero reference values, $e = -\theta$. The upper plots (a) and (b) correspond to the case without gravity, and the lower plots (c) and (d) to the case with gravity. The non-hysteresis case (32) is shown in the left-hand plots (a) and (c), and the hysteresis case (35) is shown in the right-hand plots (b) and (d). With the same classification of all four cases, the joint torsion phase portrait, in the $(x, \dot{x})$ coordinates, is shown in Fig. 7. All four cases indicate a moderate oscillation of the joint torsion, which converges to an equilibrium of
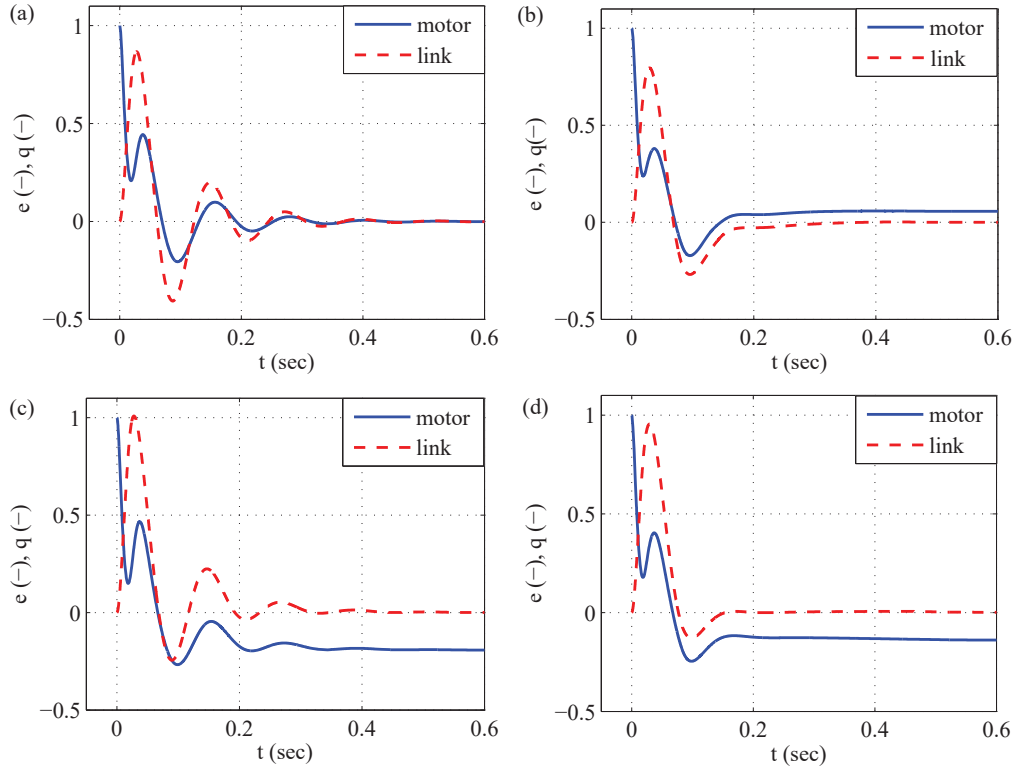
Fig. 6. Motor and link position response: (a) non-hysteresis non-gravity, (b) hysteresis non-gravity, (c) non-hysteresis gravity, (d) hysteresis gravity.

the control error. Recall that in both, gravity and hysteresis cases, it is the link position and not the motor one that reaches the zero steady-state, thus confirming that VTS is able to compensate for the joint torsion errors. Here one should keep in mind that the primary goal of (virtual) torsion sensing is to improve the link positioning accuracy, while the motor position can deviate from zero steady-state and take explicitly into account the relative joint torsion.

6. CONCLUSIONS
The absolute stability of including the virtual torsion sensor (VTS) into position control loop of the flexible robotic joints has been discussed and demonstrated. The provided analysis exposed the dissipativity and sector-conditioned passivity of the torsion-torque hysteresis map. With two boundary cases of zero and maximal energy dissipation per reversal cycle, the absolute stability in the Popov sense has been proven after providing an appropriate loop transformation. Numerical examples have visualized the results and the applicability of VTS within the joint position control of robotic manipulators with nonlinear and memory affected elasticities. The overall development aims contributing to more advanced control in flexible and lightweight robotics with goals of sensor reduction and enhancement of positioning accuracy.

References
1. Patrik Axelsson, Rickard Karlsson, and Mikael Norrlöf. Bayesian state estimation of a flexible industrial robot. *Control Engineering Practice*, 20(11):1220–1228, 2012.
2. Nikita Evgen'evich Barabanov and Vladimir Andreevich Yakubovich. Absolute stability of control systems having one hysteresis-like nonlinearity. *Avtomatika i Telemekhanika*, (12):5–12, 1979.
3. Giorgio Bertotti and Isaak Mayergoyz. *The science of hysteresis*, volume 1–3. Academic Press, 2006.
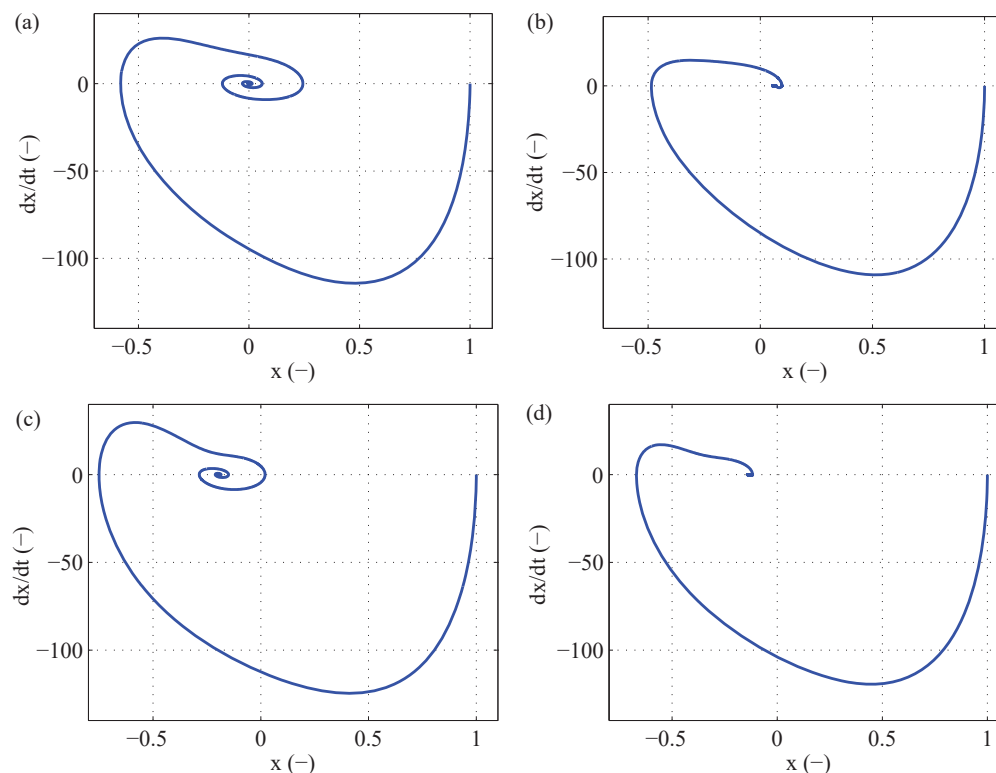
Fig. 7. Joint torsion phase portrait: (a) non-hysteresis non-gravity, (b) hysteresis non-gravity, (c) non-hysteresis gravity, (d) hysteresis gravity.

4. Christopher I Byrnes, Alberto Isidori, and Jan C Willems. Passivity, feedback equivalence, and the global stabilization of minimum phase nonlinear systems. *IEEE Transactions on Automatic Control*, 36(11):1228–1240, 1991.
5. Alessandro De Luca. Feedforward/feedback laws for the control of flexible robots. In *IEEE International Conference on Robotics and Automation (ICRA)*, volume 1, pages 233–240, 2000.
6. Alessandro De Luca. Feedforward/feedback laws for the control of flexible robots. In *IEEE International Conference on Robotics and Automation (ICRA'00)*, pages 233–240, 2000.
7. Alessandro De Luca and Raffaella Mattone. Actuator failure detection and isolation using generalized momenta. In *Proc. IEEE International Conference on Robotics and Automation (ICRA'03)*, pages 634–639, 2003.
8. Alessandro De Luca, D Schroder, and Michael Thummel. An acceleration-based state observer for robot manipulators with elastic joints. In *IEEE Int. Conference on Robotics and Automation*, pages 3817–3823, 2007.
9. Claudio De Persis and Alberto Isidori. A geometric approach to nonlinear fault detection and isolation. *IEEE Transactions on Automatic Control*, 46(6):853–865, 2001.
10. Rached Dhaouadi, Fathi Ghorbel, and Prasanna Gandhi. A new dynamic model of hysteresis in harmonic drives. *IEEE Trans. on Industrial Electronics*, 50(6):1165–1171, 2003.
11. Robert Gorbet, Kirsten Morris, and David WL Wang. Passivity-based stability and control of hysteresis in smart actuators. *IEEE Transactions on Control Systems Technology*, 9(1):5–16, 2001.
12. David John Hill and Peter James Moylan. Stability results for nonlinear feedback systems. *Automatica*, 13(4):377–382, 1977.
13. John Hung. Control of industrial robots that have transmission elasticity. *IEEE Trans. on Industrial Electronics*, 38(6):421–427, 1991.
14. Mrdjan Jankovic. Observer based control for elastic joint robots. *IEEE Trans. on Robotics and Automation*, 11(4):618–623, 1995.
15. Rafael Kelly and Víctor Santibáñez. Global regulation of elastic joint robots based on energy shaping. *IEEE Trans. on Automatic Control*, 43(10):1451–1456, 1998.
16. Manuel Keppler, Dominic Lakatos, Christian Ott, and Alin Albu-Schäffer. A passivity-based controller for motion tracking and damping assignment for compliantly actuated robots. In *IEEE 55th Conference on Decision and Control (CDC2016)*, pages 1521–1528, 2016.
17. Hassan K Khalil. *Nonlinear Systems*. Pearson, third edition, 2001.

18. Nenad Kircanski, Andrew Goldenberg, and S. Jia. An experimental study of nonlinear stiffness, hysteresis, and friction effects in robot joints with harmonic drives and torque sensors. In *Experimental Robotics III*, volume 200, pages 326–340. Springer, 1994.

19. JinHyoung Oh and Dennis Bernstein. Semilinear duhem model for rate-independent and rate-dependent hysteresis. *IEEE Transactions on Automatic Control*, 50(5):631–645, 2005.

20. Romeo Ortega, Julio Antonio Loría Perez, Per Johan Nicklasson, and Hebertt Sira-Ramirez. *Passivity-based control of Euler-Lagrange systems: mechanical, electrical and electromechanical applications.* Springer, first edition, 1998.

21. Ruiyue Ouyang and Bayu Jayawardhana. Absolute stability analysis of linear systems with duhem hysteresis operator. *Automatica*, 50(7):1860–1866, 2014.

22. Michael Ruderman. Compensation of nonlinear torsion in flexible joint robots: Comparison of two approaches. *IEEE Transactions on Industrial Electronics*, 63(9):5744–5751, 2016.

23. Michael Ruderman. On stability and robustness of virtual torsion sensor (VTS) for flexible joint robots. In *IEEE 42nd Annual Conference of the Industrial Electronics Society*, pages 6984–6899, 2016.

24. Michael Ruderman, Torsten Bertram, and Makoto Iwasaki. Modeling, observation, and control of hysteresis torsion in elastic robot joints. *Mechatronics*, 24(5):407–415, 2014.

25. Michael Ruderman and Makoto Iwasaki. On identification and sensorless control of nonlinear torsion in elastic robotic joints. In *IEEE 40th Anual Conference Industrial Electronics Society*, pages 2828–2833, 2014.

26. Michael Ruderman and Makoto Iwasaki. Sensorless torsion control of elastic joint robots with hysteresis and friction. *IEEE Transactions on Industrial Electronics*, 63(3):1889–1899, 2015.

27. Michael Ruderman and Makoto Iwasaki. On damping characteristics of frictional hysteresis in pre-sliding range. In *Journal of Physics: Conference Series*, volume 727, page 012014, 2016.

28. Michael Ruderman and Dmitrii Rachinskii. Use of Prandtl-Ishlinskii hysteresis operators for coulomb friction modeling with presliding. In *Journal of Physics: Conference Series*, volume 811, page 012013, 2017.

29. Bruno Siciliano and Oussama Khatib. *Springer handbook of robotics.* Springer, 2016.

30. Bruno Siciliano, Lorenzo Sciavicco, Luigi Villani, and Giuseppe Oriolo. *Robotics: modelling, planning and control.* Springer, 2009.

31. Jean-Jacques Slotine and Weiping Li. *Applied Nonlinear Control.* Prentice Hall, 1991.

32. Mark Spong. Modeling and control of elastic joint robots. *Journal of Dynamic Systems, Measurement, and Control*, 109(4):310–319, 1987.

33. Mark Spong, Seth Hutchinson, and Mathukumalli Vidyasagar. *Robot modeling and control.* Wiley, 2006.

34. Hamid Taghirad and Pierre Belanger. Modeling and parameter identification of harmonic drive systems. *Journal of Dynamic Systems, Measurement, and Control*, 120(4):439–444, 1998.

35. Patrizio Tomei. A simple PD controller for robots with elastic joints. *IEEE Transactions on Automatic Control*, 36(10):1208–1213, 1991.

36. Jan C Willems. Dissipative dynamical systems part I: General theory. *Archive for rational mech. and anal.*, 45(5):321–351, 1972.

37. Sebastian Wolf, Giorgio Grioli, Oliver Eiberger, Werner Friedl, Markus Grebenstein, Hannes Höppner, Etienne Burdet, Darwin G Caldwell, Raffaella Carloni, Manuel G Catalano, et al. Variable stiffness actuators: Review on design and components. *IEEE/ASME Transactions on Mechatronics*, 21(5):2418–2430, 2016.